Blob population dynamics during immiscible two-phase flows in reconstructed porous media

A. G. Yiotis, L. Talon, and D. Salin
Laboratoire FAST, Univ. Pierre & Marie Curie, Univ. Paris-Sud, CNRS, Orsay 91405, France
(Received 30 October 2012; published 4 March 2013)

We study the dynamics of nonwetting liquid blobs during immiscible two-phase flows in stochastically reconstructed porous domains predominantly saturated by a wetting fluid. The flow problem is solved explicitly using a Lattice-Boltzmann model that captures both the bulk phase and interfacial dynamics of the process. We show that the nonwetting blobs undergo a continuous life cycle of dynamic breaking up and coalescence producing two populations of blobs, a mobile and a stranded one, that exchange continuously mass between them. The process reaches a "steady state" when the rates of coalescence and breaking up become equal, and the macroscopic flow variables remain practically constant with time. At steady state, mass partitioning between mobile and immobile populations depends strongly on the applied Bond number Bo and the initial nonwetting phase distributions. Three flow regimes are identified: a single-phase flow Darcy-type regime at low Bo numbers, a non-Darcy two-phase flow regime at intermediate values of Bo, where the capillary number scales as $\mathrm{Ca} \propto \mathrm{Bo}^2$, and a Darcy-type two-phase flow regime at higher values of Bo. Our numerical results are found to be in good agreement with recent experimental and theoretical works.

DOI: 10.1103/PhysRevE.87.033001 PACS number(s): 47.56.+r, 47.55.dd

I. INTRODUCTION

Immiscible two-phase flow in soils is a subject of significant scientific and technological interest. It is encountered in a series of environmental and energy-related processes, such as the remediation of soils contaminated with toxic anthropogenic chemicals, secondary and enhanced oil recovery (EOR) from fractured petroleum reservoirs, and the geological storage of CO_2 in deep saline aquifers and depleted oil reservoirs, among others. From a technological and/or environmental aspect, the objectives of such processes is either the recovery of fluids that pose environmental dangers due to infiltration into the drinking water table (such as in soil remediation), the recovery of fluids of financial interest (such as in oil recovery), or the geological storage of by-product fluids, replacing the space otherwise occupied by subsurface water in the Vadose and saturated zones (such as in CO_2 sequestration).

Typically, the recovery of such fluids [otherwise collectively called Non-Aqueous Phase Liquids (NAPLs), as opposed to the continuous aqueous phase which is dominant is the subsurface] is accomplished by introducing purge or flush fluids (steam, water, CO_2, or natural gas) from injection wells in order to displace NAPLs towards production wells. These recovery technologies aim at increasing pressure gradients in the soil and producing flow conditions that overcome capillary forces at the pore scale. Other technologies rely on the reduction of the interfacial tension between NAPLs and the aqueous phase using surfactant or generating miscible flow conditions [1–3].

During recovery, as the NAPL phase saturation in the soil progressively decreases, the NAPL phase becomes highly discontinuous by breaking up in smaller droplets or blobs (otherwise called ganglia) that may span across several pore volumes. The randomness and heterogeneity of the pore space within soil formations lead to the production of blob size distributions that either flow under the combined effect of capillary, viscous, and gravity or buoyancy forces or become stranded in lower permeability regions of the soil. The recovery of such trapped residuals, which may account for a significant amount of the initial NAPL saturation, is the aim of enhanced recovery technologies, involving blob remobilization and/or dissolution based on targeted flushes of dissolution agents and surfactants. Eventually, the relative magnitude of the forces acting on the blob interfaces at the pore and pore-network scales determines their fate at the field scale, either mobile or stranded, and the recovery potential of the applied technology. Blob size distributions and local flow conditions determine also the available interfacial areas and effective mass transport coefficients, which are crucial parameters in recovery technologies involving NAPL dissolution or volatilization.

Several methods have been proposed to model the dynamics of NAPL blobs during immiscible two-phase flows in porous media by accounting for pore-scale physics. These methods include pore network modeling [4–9], stochastic simulation [10,11], mechanistic modeling [12], and the recently developed method of Darcian dynamics [13]. Essentially all these approaches treat the flow problem and the interfacial dynamics at the pore scale, since continuum scale approaches, which are based on relative permeability considerations, will fail to accurately describe the process due to the highly discontinuous nature of the nonwetting phase, interfacial instabilities that may arise under certain flow conditions, and the potential heterogeneity of the porous medium. The characteristic of these pore scale methods is that they rely on simplified mechanistic rules to determine the probability of fluid-fluid interfaces invading the pores of the medium. These rules typically take into account the effect of capillary, viscous, and gravity forces across interfaces as they move through pore volumes. Viscous forces and the pressure field are calculated by solving linear flow models, such as Poiseuille or Darcy-type equations, through simplified void topologies such as pore networks [4], or continuous permeability fields [13]. Capillary forces at the pore throats are calculated through Laplace's law. These approximations, although crude, have provided the means to qualitatively model blob population dynamics at a reasonable computational cost. On the other hand, application of such models is limited to simplified pore geometries, and

their accuracy is questionable given that the flow and interfacial physics involved are coupled in macroscopic parameters, such as relative permeabilities, or coalescence probabilities [6].

In recent years, the continuous development of rigorous lattice Boltzmann (LB) models of multiphase, multicomponent systems, in conjunction with the significant increase in computational power, has allowed for modeling immiscible two-phase flows in more realistic pore structures [14–16]. This allows for the deterministic description of the flow problem and the interfacial dynamics at the pore scale, providing significant insight into the effects of pore scale physics on the macroscopic or continuum dynamics in such systems. However, the main focus of these earlier studies was on the construction of relative permeability curves, rather than on the flow conditions that lead to the mobilization of trapped NAPL residuals in porous media.

In this paper we focus on the conditions that lead to the trapping and mobilization of the disconnected NAPL blobs by applying an immiscible LB model for flow driven by gravity in a stochastically reconstructed porous domain. Emphasis is placed on the effects of the medium structure, flow conditions, and saturations on the population dynamics of NAPLs during transient and "steady-state" conditions, blob size distributions, the ratio of mobile to stranded populations, and the resulting interfacial areas. The effects of the initial blob size distributions on the resulting steady-state conditions are also investigated. For simplicity, calculations are performed on a two-dimensional (2D) reconstructed porous domain with a relatively high porosity. Extension of the method to three-dimensional (3D) porous domains is straightforward, but requires significant computational resources.

II. MODEL FORMULATION

The model used for the study of NAPL blob dynamics in soils consists of a LB model to solve for the dynamics of immiscible flow in the pore space, a stochastic reconstruction algorithm for representing the pore space, and appropriate boundary conditions at the fluid-solid walls to account for wettability and capillary effects. These components will be described in detail in the following sections.

A. Lattice Boltzmann model

We solve for the hydrodynamics of immiscible two-phase flow in porous media using an appropriate LB model in a discrete permeability field. Following the work of He *et al.* [17], the continuous Boltzmann equation for nonideal dense fluids can be written in the following form:

$$\frac{Df}{Dt} = \frac{\partial f}{\partial t} + \vec{\xi}\cdot\frac{\partial f}{\partial \vec{x}} - \frac{1}{\lambda}(f - f^{\mathrm{eq}}) + \frac{\vec{F}\cdot(\vec{\xi}-\vec{u})}{\rho RT} f^{\mathrm{eq}}, \quad (1)$$

where $f(\vec{x},\vec{\xi},t)$ is the single particle distribution function, $\vec{\xi}$ and $\vec{u}$ are the microscopic and macroscopic local velocity vectors, respectively, ρ is the macroscopic density, $\vec{x}$ is the position vector, λ is a relaxation time related to the kinematic viscosity as $\nu = RT\lambda$, $\vec{F}$ is the force experienced by fluid particles, R is the ideal gas constant, T is the temperature, and $f^{\mathrm{eq}}(\vec{u})$ is the single particle distribution function at thermodynamic equilibrium, which follows a Maxwell-Boltzmann distribution.

Equation (1) can be solved following the LB Lagrangian-based discretization scheme by integrating in the microscopic velocity space $\vec{\xi}$ and time t (i.e., as shown in Refs. [18,19]):

$$\begin{aligned} &f_i(\vec{x}+\vec{\xi}_i\delta t, t+\delta t) - f_i(\vec{x},t) \\ &= -\int_{\vec{x},t}^{\vec{x}+\vec{\xi}_i\delta t, t+\delta t} \frac{1}{\lambda}\left(f_i - f_i^{\mathrm{eq}}\right) dt' \\ &\quad + \int_{\vec{x},t}^{\vec{x}+\vec{\xi}_i\delta t, t+\delta t} \frac{\vec{F}\cdot(\vec{\xi}_i-\vec{u})}{\rho RT} f_i^{\mathrm{eq}}\, dt' \\ &= \frac{1}{2}\left[-\frac{1}{\tau}\left(f_i - f_i^{\mathrm{eq}}\right) + \frac{\vec{F}\cdot(\vec{\xi}_i-\vec{u})}{RT}\Gamma_i\delta t\right]_{\vec{x},t} \\ &\quad + \frac{1}{2}\left[-\frac{1}{\tau}\left(f_i - f_i^{\mathrm{eq}}\right) + \frac{\vec{F}\cdot(\vec{\xi}_i-\vec{u})}{RT}\Gamma_i\delta t\right]_{\vec{x}+\vec{\xi}_i\delta t, t+\delta t}, \end{aligned} \quad (2)$$

where $\Gamma_i(\vec{u}) = f_i^{\mathrm{eq}}(\vec{u})/\rho$, $\tau = \lambda/\delta t$, and δt is the time step. The discretized equilibrium distribution function f^{eq} is derived from the Maxwell-Boltzmann distribution by a Taylor expansion in terms of the Mach number, $\vec{u}/c_s = \vec{u}/\sqrt{RT}$:

$$f_i^{\mathrm{eq}}(\vec{u}) = w_i\rho\left[1 + \frac{\vec{\xi}_i\cdot\vec{u}}{c_s^2} + \frac{(\vec{\xi}_i\cdot\vec{u})^2}{2c_s^4} - \frac{\vec{u}\cdot\vec{u}}{2c_s^2}\right], \quad (3)$$

where w_i are appropriate weights that depend on the selected discretization scheme.

In the resulting LB equation, time integration in $[t,t+\delta t]$ is coupled with the space integration in $[\vec{x},\vec{x}+\vec{\xi}_i\delta t]$. The LBE can be made explicit by the following transformation for f:

$$\bar{f}_i = f_i - \frac{\vec{F}\cdot(\vec{\xi}_i-\vec{u})}{RT}\Gamma_i\frac{\delta t}{2}, \quad (4)$$

which yields the following evolution equation for $\bar{f}$:

$$\begin{aligned} &\bar{f}_i(\vec{x}+\vec{\xi}_i\delta t, t+\delta t) \\ &= \bar{f}_i(\vec{x},t) - \frac{\bar{f}_i(\vec{x},t) - f_i^{\mathrm{eq}}(\vec{x},t)}{\tau'} \\ &\quad + \frac{2\tau'-1}{\tau'}\frac{(\vec{\xi}_i-\vec{u})\cdot\vec{F}}{RT}\Gamma_i(\vec{u})\delta t \end{aligned} \quad (5)$$

where $\tau' = \tau + 1/2$ and $\nu = RT(\tau'-1/2)\delta t$.

Phase separation is then induced by incorporating an appropriate expression for the intermolecular force $\vec{F}$ in Eq. (5). For a van der Waals fluid, for instance, the intermolecular force $\vec{F}$ can be obtained through a mean-field approximation and accounting for exclusion volume effects [20,21] as follows:

$$\vec{F} = -\vec{\nabla}(p_0 - \rho RT) + \rho\kappa\vec{\nabla}\nabla^2\rho = -\vec{\nabla}\Psi_p + \vec{F}_s, \quad (6)$$

where p_0 is the thermodynamic pressure, Ψ_p is the divergence from the ideal pressure, $\vec{F}_s$ accounts for interfacial forces, and κ is a parameter associated with the intermolecular potential u_{attr} as

$$\kappa = -\frac{1}{6}\int_{r>\sigma} r^2 u_{\mathrm{attr}}(r)\, d\vec{r}, \quad (7)$$

where σ is the molecular diameter.

Equation (6), which is usually referred to as the potential form of the forcing expression, can be also expressed in terms

of the chemical potential of the bulk phases μ_0 through the Gibbs-Duhem equation $\vec{\nabla}P_0 = \rho\vec{\nabla}\mu_0$ [18]:

$$\begin{aligned}\vec{F} &= -\rho\vec{\nabla}\mu_0 + \vec{\nabla}\rho RT + \rho\kappa\vec{\nabla}\nabla^2\rho \\ &= -\rho\vec{\nabla}(\mu_0 - \kappa\nabla^2\rho - RT\ln\rho) \\ &= -\rho\vec{\nabla}(\mu - RT\ln\rho) = -\rho\vec{\nabla}\Psi_\mu. \end{aligned} \tag{8}$$

In the above expression we note that $\mu_0^{\text{ideal}} = RT\ln\rho$ corresponds to the bulk chemical potential of the ideal gas and $\mu = \mu_0 - \kappa\nabla^2\rho$. The latter formulation of the potential form is adopted in the present contribution as it has been shown to provide increased numerical stability and can better handle mass separation between phases [19].

In order to improve the numerical stability of the LBE scheme of Eqs. (5)–(8), He *et al.* [21] introduced a second single particle distribution function g as follows:

$$g = fRT - \Psi_p'(\rho)\Gamma(0). \tag{9}$$

This produced the following evolution equation:

$$\begin{aligned}&\bar{g}_i(\vec{x} + \vec{\xi}_i\delta t, t + \delta t) \\ &= \bar{g}_i(\vec{x},t) - \frac{\bar{g}_i(\vec{x},t) - g_i^{\text{eq}}(\vec{x},t)}{\tau'} \\ &\quad + \frac{2\tau' - 1}{\tau'}(\vec{\xi}_i - \vec{u})\cdot\{\Gamma_i(\vec{u})(\vec{F}_s' + \vec{F}_b) \\ &\quad - [\Gamma_i(\vec{u}) - \Gamma_i(0)]\vec{\nabla}\Psi_p'\}\delta t, \end{aligned} \tag{10}$$

where

$$\begin{aligned}\bar{g}_i &= g_i - \tfrac{1}{2}(\vec{\xi}_i - \vec{u})\cdot\{\Gamma_i(\vec{u})(\vec{F}_s' + \vec{F}_b) \\ &\quad - [\Gamma_i(\vec{u}) - \Gamma_i(0)]\vec{\nabla}\Psi_p'\}\delta t \end{aligned} \tag{11}$$

and

$$g_i^{\text{eq}}(\vec{u}) = w_i\left\{p + \rho c_s^2\left[\frac{\vec{\xi}_i\cdot\vec{u}}{c_s^2} + \frac{(\vec{\xi}_i\cdot\vec{u})^2}{2c_s^4} - \frac{\vec{u}\cdot\vec{u}}{2c_s^2}\right]\right\}. \tag{12}$$

$\vec{F}_b$ accounts for body forces acting on fluid particles, such as gravity $\vec{F}_b = \rho\vec{g}$, which is considered in this study to drive fluid flow. Note that body forces are not accounted for in Eq. (5) since this equation is used only to track the phase field. Here we have also defined Ψ_p' following a different rearrangement of the forcing terms in Eq. (6) proposed by Ref. [18], known as the stress form of the forcing terms:

$$\begin{aligned}\vec{F} &= -\vec{\nabla}\Psi_p' + \vec{F}_s' \\ &= -\vec{\nabla}\left(p_0 - \rho RT - \kappa\rho\nabla^2\rho + \frac{\kappa}{2}\vec{\nabla}\rho\cdot\vec{\nabla}\rho\right) \\ &\quad + \kappa\vec{\nabla}(\rho\nabla^2\rho) - \frac{\kappa}{2}\vec{\nabla}(\vec{\nabla}\rho\cdot\vec{\nabla}\rho) + \kappa\vec{\nabla}(\vec{\nabla}\rho\cdot\vec{\nabla}\rho) \\ &\quad - \kappa\vec{\nabla}\cdot(\vec{\nabla}\rho\vec{\nabla}\rho). \end{aligned} \tag{13}$$

This expression removes unphysical discontinuities in the pressure field across the the interface and reduces spurious velocity currents in the vicinity of the interface.

The above model is thermodynamically consistent for the specific case of van der Waals (vdW) fluids, as long as the thermodynamic pressure and/or chemical potential is calculated using the vdW equation of state [19,22]. In this case, Eq. (5) can be solved directly to calculate the liquid and vapor phase densities of a vdW fluid in very good agreement with the vdW theory and the corresponding Maxwell equal area rule [23]. The interfacial tension is then predicted by van der Waals theory by integrating over the density profile across the interface:

$$\gamma = \int_{-\infty}^{+\infty}\kappa\left(\frac{d\rho}{dx}\right)^2 dx. \tag{14}$$

Note that for a vdW fluid, κ is a dependent variable and cannot take arbitrary values.

The above scheme can be also applied to model the hydrodynamics of any arbitrary pair of fluids with densities ρ_{nw} and ρ_w using the vdW density field as a phase index and interpolating the desired densities values over the corresponding vdW densities [21]. The phase field φ is thus evaluated by integrating $\bar{f}$ in the microscopic velocity space:

$$\varphi(\vec{x},t) = \sum_i \bar{f}_i(\vec{x},t) \tag{15}$$

and the macroscopic density field as

$$\rho = \rho_{nw} + \frac{\varphi - \varphi_l}{\varphi_h - \varphi_l}(\rho_w - \rho_{nw}), \tag{16}$$

where φ_h,φ_l are the highest and lowest values of the index function φ calculated by Eq. (15).

The interfacial tension of the simulated pair of fluids is tuned by treating κ as an adjustable parameter. Equation (14) remains valid in this approach.

Then the macroscopic velocity and pressure are

$$RT\rho\vec{u}(\vec{x},t) = \sum_i \bar{g}_i(\vec{x},t)\vec{\xi}_i + \frac{RT\delta t}{2}(\vec{F}_s' + \vec{F}_b), \tag{17}$$

$$p(\vec{x},t) = \sum_i \bar{g}_i(\vec{x},t) - \frac{1}{2}\vec{u}(\vec{x},t)\cdot\vec{\nabla}\Psi_\mu(\rho)\delta t. \tag{18}$$

In the present paper we use the vdW equation of state in reduced form to induce phase separation without loss of generality of the method:

$$p_0 = \frac{\rho RT}{1 - b\rho} - a\rho^2, \tag{19}$$

where $a = \frac{9}{8}T_c/\rho_c$, $b = 1/(3\rho_c)$, $T_c = RT/T_r$, and $\rho_c = 1$ for simplicity.

The corresponding bulk phase chemical potential μ_0 is calculated by solving the following equation for the bulk phase energy E_0:

$$p_0 = \rho\mu_0 - E_0, \quad \text{where} \quad \mu_0 = \frac{\partial E_0}{\partial\rho}. \tag{20}$$

This yields

$$\mu_0 = RT\ln\left(\frac{\rho}{1 - b\rho}\right) + \frac{RT}{1 - b\rho} - 2a\rho. \tag{21}$$

An alternative approach to the one used here consists of using an *ad hoc* equation of state (instead of the vdW) for controlling fluid densities, interfacial tension, and thickness without other adjustable parameters [18,24].

In this study we perform 2D LB simulations using a D2Q9 discretization scheme, where the microscopic velocity $\vec{\xi}$ is discretized in nine vectors (including the null vector), defined

as follows:

$$\vec{\xi}_i = \begin{cases} (0,0)c & i = 0 \\ (\pm 1,0)c & i = 1,2 \\ (0,\pm 1)c & i = 3,4 \\ (\pm 1,\pm 1)c & i = 5,6,7,8, \end{cases} \tag{22}$$

where we take $c = \delta x/\delta t$ equal to unity here for simplicity and δx is the lattice spacing. Assuming the molar mass equal to unity and recalling that the equation of state for the ideal gas is $p = \rho c_s^2$, where $c_s^2 = RT$ is the speed of sound, then the product RT in lattice units can be expressed by $RT = c^2/3$ [25]. The corresponding integral weights for Eqs. (3) and (12) are

$$w_i = \begin{cases} 4/9 & i = 0 \\ 1/9 & i = 1,2,3,4 \\ 1/36 & i = 5,6,7,8. \end{cases} \tag{23}$$

A crucial factor for numerical stability and mass conservation, particularly in smaller blobs, is the appropriate selection of the discretization scheme for spatial derivatives. Here spatial derivatives (both directional and nondirectional), i.e., of density ρ, are calculated using a central isotropic discretization scheme according to Refs. [18,24] as follows:

$$\vec{\nabla}\rho|_{\vec{x}} = \sum_{i\neq 0} \frac{w_i \vec{\xi}_i [\rho(\vec{x} + \vec{\xi}_i \delta t) - \rho(\vec{x} - \vec{\xi}_i \delta t)]}{2RT\delta t}, \tag{24}$$

$$\nabla^2 \rho|_{\vec{x}} = \sum_{i\neq 0} \frac{w_i [\rho(\vec{x} + \vec{\xi}_i \delta t) - 2\rho(\vec{x}) + \rho(\vec{x} - \vec{\xi}_i \delta t)]}{RT\delta t^2}. \tag{25}$$

The components of $\vec{\nabla}\rho$ are calculated as $\frac{\partial \rho}{\partial x_j}|_{\vec{x}} = \vec{\nabla}\rho(\vec{x}) \cdot \vec{e}_j$, where $\vec{e}_j$ is the unit vector in j direction.

To conclude this section, it is important to note that in the present paper we have used a single relaxation time scheme (BGK model) to approximate the collision operator in the Boltzmann equation for the sake of simplicity. This scheme, coupled with the bounce-back rule at solid-fluid interfaces to recover no-slip boundary conditions, is known to produce a dependence of the effective location of the wall on the kinematic viscosity, namely, on the selected value of the relaxation parameter τ' [26–28]. This scheme was used here while keeping the kinematic viscosity constant and equal for both phases. A multiple-relaxation scheme could be alternatively used, in order to have identical boundaries effects for both phases, independently of the selected values of the kinematic viscosities.

B. Wettability effects

The above described LB model does not explicitly account for intermolecular forces between fluid and solid molecules at fluid-solid interfaces, namely, at pore walls. The bounce-back boundary condition is applied to all fluid particles when they collide with a solid wall. Wettability effects are incorporated in our LB simulations by implementing soild-fluid boundary conditions as described in one of our previous works [29]. We account for attracting (adhesive) forces between fluid particles and molecules of the solid surface by assigning an effective value for the density of the solid sites in the range between ρ_w and ρ_{nw}, depending on whose phases molecules are attracted stronger by the molecules of the solid surface. The density assigned to the solid lattice sites enters the calculations through the interfacial force $\vec{F}_s$. This boundary condition gives rise to capillarity effects as fluid-fluid interfaces move within pore walls, and it is used to modify the contact angle of the interface at the solid surface [29]. In this study we assume a perfectly wetting fluid ρ_w (contact angle $\theta = 0$), and we thus set the solid site density $\rho_s = \rho_w$.

C. Stochastically reconstructed porous domains

The porous medium in our study is represented by 2D porous domains in the form of discrete permeability fields of size $1024^2 \delta x^2$. Each domain consists of solid (impermeable) and void (permeable) sites, where the spatial distribution of the solid sites is accomplished using a stochastic reconstruction algorithm that pursues the recovery of the statistical properties of naturally occurring porous media, i.e., sandstone, typically the porosity ϕ and the two-point autocorrelation function [30,31].

The porous medium is thus generated using a standard spectral method. First, we generate a matrix $W(\vec{r})$ of white random noise (with zero mean and a standard deviation of one). Then we compute the Fourier transform $Z(\vec{r})$, which we multiply with a Gaussian function, yielding

$$Z'(\vec{k}) = \alpha Z(\vec{k}) e^{-\frac{|\vec{k}|^2}{k_0^2}}. \tag{26}$$

A fast inverse Fourier transform $f(\vec{r}) = {F_T}^{-1}(Z'(\vec{k}))$ leads then to a Gaussian distributed noise correlated with a Gaussian correlation function:

$$F_T(ff^*) = \alpha^2 e^{-2\frac{|\vec{k}|^2}{k_0^2}},$$

which leads to the autocorrelation function:

$$(f^* f)(x) \propto e^{-\frac{k_0^2}{8}x^2} = e^{-\frac{1}{2}(\frac{\pi x}{2\lambda_s})^2}, \tag{27}$$

where $\lambda_s = \pi/k_0$ and * denotes the convolution product. Without loss in generality, the prefactor α is set to have a standard deviation equal to one. The solid lattices are obtained by level setting the field $f(\vec{r})$ with a given value, f_0: $S = \{\vec{r}|f(\vec{r}) < f_0\}$. The porosity is then directly related to the cumulative distribution function, $P(f)$, which is by construction an error function centered around 0 and of standard deviation equal to 1:

$$f_0 = P^{-1}(\phi).$$

The above procedure allows for the construction of porous domains parametrized by the porosity ϕ and the correlation length λ_s for the spatial distribution of the solid sites. Given the 2D nature of the domains, a high porosity value $\phi = 0.8$ and $\lambda_s = 15\delta x$ are selected in order to construct percolating domains in all directions (see Fig. 1).

It straightforward to show that the superficial (Darcy) velocity of a liquid flowing in such a domain is proportional to the applied body force $\vec{F}_b$ by solving the previously described LB scheme for single phase flow (namely, $S_w = 1$). The permeability of the medium K, determined by Darcy's law, is then found to scale with the correlation length of the solid sites as $K \propto \lambda_s^2$; namely, λ_s can be used as a proxy for the average pore size.

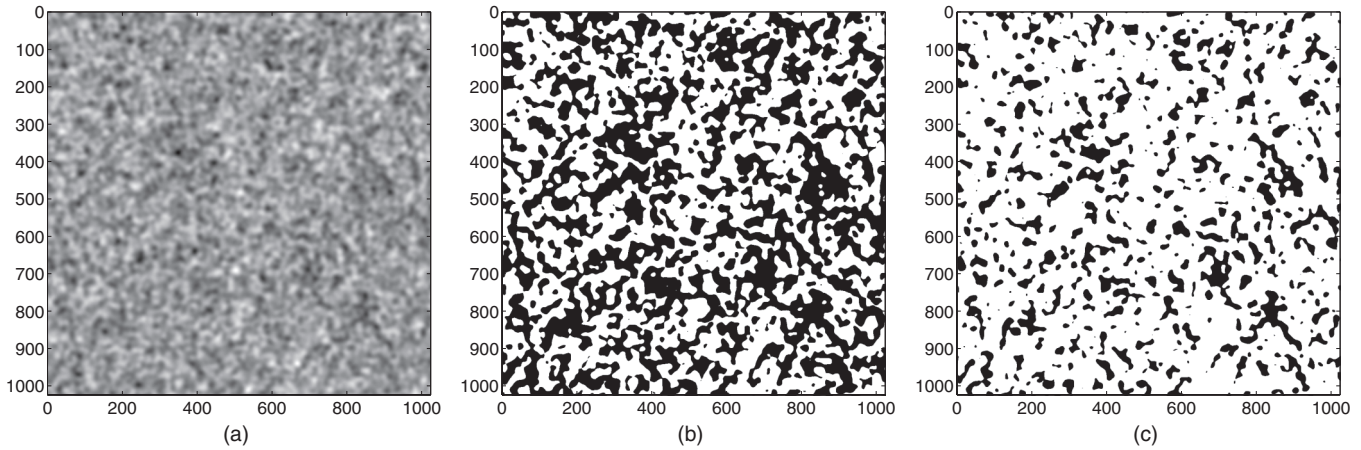

FIG. 1. 2D stochastically reconstructed porous domain with $\lambda_s = 15\delta x$. (a) Continuous permeability field with darker colors indicating less permeable sites (or equivalently higher probability of solid phase). (b) Discrete permeability field with $\phi = 0.55$. Black and white colors represent solid and void phases, respectively. (c) Discrete permeability field with $\phi = 0.8$, which is used for typical simulations presented in this study. Note that for values of $\phi < 0.5$ the domain is not percolating in all directions.

III. NUMERICAL SIMULATIONS

We performed a series of numerical simulations in 2D porous domains with porosities $0.7 \leqslant \phi \leqslant 0.9$, constructed as described in the previous section, and saturated with two immiscible fluids. The nonwetting phase saturation was taken $S_{nw} \leqslant 0.3$ in our simulations. The initial nonwetting phase distribution patterns were generated using a similar reconstruction algorithm as the one described above for the porous medium. As previously, a Gaussian field $h(\vec{r})$ is first generated, parametrized by the correlation length λ_{nw} for the sites occupied by the nonwetting phase. However, the level set method differs slightly from the one used for the solid site distribution, since one now needs to take into account that some sites are already occupied by solid. The nonwetting phase region is now defined as $\mathrm{NW} = \{\vec{r} \mid \vec{r} \notin S; h(\vec{r}) < h_0\}$. Practically, $h(\vec{r})$ is set to a very high value at solid cites. Since the cumulative is not known analytically, we used an ordering procedure to determine the level set value h_0, in order to impose the desired nonwetting saturation S_{nw}. By ordering the value field $h(\vec{r}) \rightarrow H[k]$, $k = 1, \ldots, N$, where N is the total number of grid points, we deduce the level set value by $h_0 = H[N\phi S_{nw}]$.

The resulting initial nonwetting phase distribution patterns for different values of the correlation length λ_{nw} are shown in Fig. 2 for a fixed value of $S_{nw} = 0.2$. It is evident that larger values of λ_{nw} lead to larger but fewer blobs initially in the domain. A Hoshen-Kopelman algorithm [32] is then applied to calculate the number, size, and interfacial area of the disconnected blobs at each time step. Figure 3 shows the initial blob size distribution in the same domain for different values of S_{nw} and $\lambda_{nw} = 15\delta x$. The distribution resembles a log-normal with a mean blob area of the order of $O(\lambda_{nw}^2)$, as expected. Here the blob size s_b is expressed in λ_{nw}^2 units, rather than lattice units δx^2, and thus negative x-axis values correspond to blob sizes less than the average pore size (given that here $\lambda_s = \lambda_{nw}$). A shift of the distribution towards larger

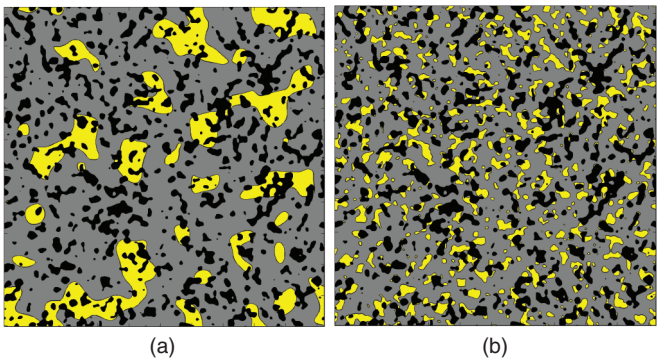

FIG. 2. (Color online) Initial phase distribution patterns for $\lambda_{nw} = 60\delta x$ (a) and $\lambda_{nw} = 15\delta x$ (b) for a medium with porosity $\phi = 0.8$, $\lambda_s = 15\delta x$, and $S_{nw} = 0.2$. Nonwetting phase blobs are shown in yellow (brighter color in gray scale), wetting phase in gray, and solid sites in black.

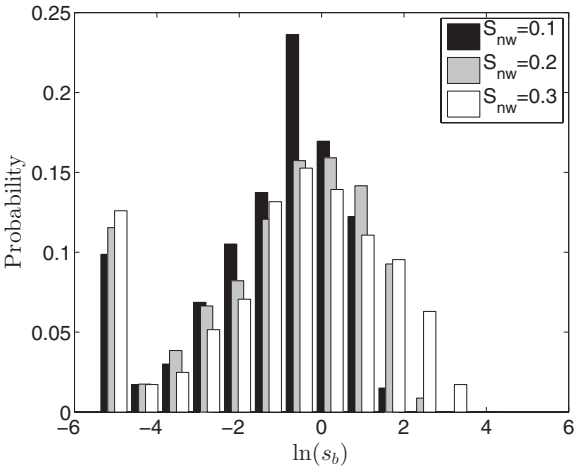

FIG. 3. Initial blob size distribution for different nonwetting phase saturations S_{nw}, and $\lambda_{nw} = \lambda_s = 15\delta x, \phi = 0.8$. The horizontal axis shows the natural logarithm of the blob size s_b (in units of λ_s^2). A mainly log-normal size distribution is observed that shifts towards larger blobs as S_{nw} increases.

sizes is also observed with increasing S_{nw} due to overlapping of smaller blobs in the finite void space.

A constant gravitational force $\vec{F}_b = \rho\vec{g}$ is then applied to generate flow through the reconstructed $1024^2\delta x^2$ porous domain, where $\vec{g}$ is the gravity acceleration vector. Periodic boundary conditions are considered in both directions. For simplicity, we take a value of $T_r = 0.95$ in Eq. (19), which yields $\varphi_l = 0.579\rho_0$ and $\varphi_h = 1.461\rho_0$ for a vdW fluid, where ρ_0 is a reference density in our system. We use these values for the wetting and nonwetting fluids in our system, namely, $\rho = \varphi$ [and thus the macroscopic density is calculated directly from Eq. (15)], since this density ratio is convenient for the simulation of an aqueous and an oily phase. The kinematic viscosity is taken again equal in both phases with $\tau' = 0.8$ and $\nu = 0.1\delta x^2/\delta t$. The interfacial tension is controlled by the adjustable parameter κ in Eq. (14), which we take here equal to $\kappa = 3 \times 10^{-2} c\delta x^2/\rho_0$. This produces an interfacial tension $\gamma = 3.2 \times 10^{-3}\rho_0 c^2\delta x$, as calculated from Eq. (14) [19,29].

The flow problem is typically characterized by two dimensionless numbers: the capillary number $\mathrm{Ca} = q\mu_e/\gamma$, which expresses the ratio of viscous over capillary forces across interfaces, and the Bond number $\mathrm{Bo} = g(\rho_w - \rho_{nw})\lambda_s^2/\gamma$, which expresses the ratio of gravity over capillary forces. Here ρ_w, ρ_{nw} are the densities of the wetting and nonwetting (or NAPL) phases, γ is the fluid-fluid interfacial tension, μ_e is an effective saturation-weighted viscosity defined as $\mu_e = S_{nw}\mu_{nw} + (1 - S_{nw})\mu_w$, and $q = q_w + q_{nw}$ is the total superficial (Darcy) velocity, where

$$q_i = \frac{1}{A}\int_A \vec{u}_i \cdot \vec{n} dA, \quad i = w,nw. \tag{28}$$

In the above equation $\vec{n} = \frac{\vec{g}}{|\vec{g}|}$ is the unit vector in the direction of the applied body force. Note that $A = A_w \cup A_{nw} \cup A_s$, where A_w, A_{nw}, and A_s are the domain sites occupied by the wetting, nonwetting, and solid phases, respectively. The evolution of the phase distribution patterns with time for a typical simulation is shown in Fig. 4. Starting from a spatially random distribution of the nonwetting phase blobs with an average size proportional to λ_{nw}^2 and random shape at $t = 0$ (see Fig. 3), all the blobs, with an initial size smaller than the average pore size, flow practically unobstructed in the void of the pores in the direction of the applied body force. The effects of capillary forces across fluid-fluid interfaces on the flow of these blobs are practically negligible. At later times, however, as blobs larger than the average pore size are formed (resulting from collisions between neighboring blobs), the effect of capillarity becomes progressively important in the resulting flow patterns and leads to the stranding of blobs in smaller pores, particularly for lower values of the applied Bo.

The increasing blob size leads to another effect which is negligible at early times: Larger blobs may deform significantly due geometrical restrictions in the flow paths as they "squeeze" through narrower pores under the effects of gravity, viscous, and capillary forces. This deformation eventually leads to the breakup of blobs into smaller ones. Both the effects of blob coalescing and breaking up will be discussed in more detail below.

At sufficiently large times, the superficial velocities q of both phases and the number of blobs reach steady-state values

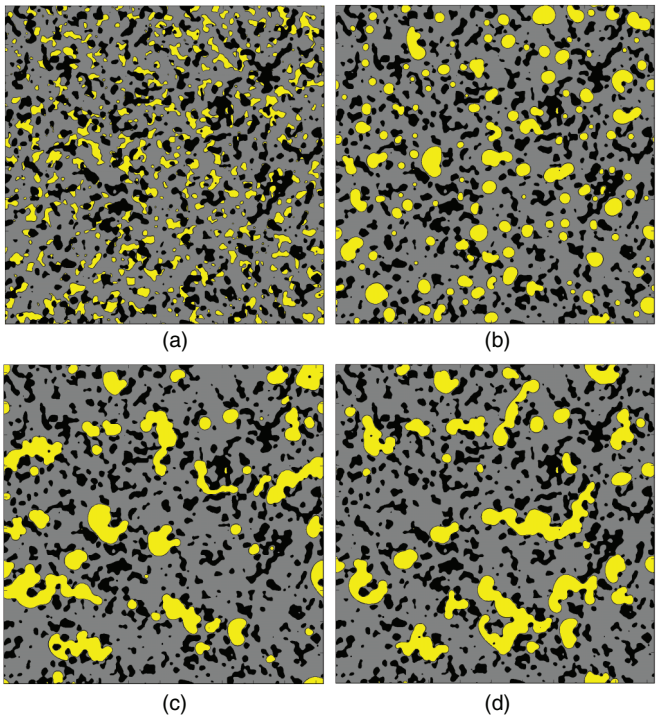

FIG. 4. (Color online) Phase distribution patterns at different time steps $t = 0$ (a), $t = 0.25 \times 10^6\delta t$ (b), $t = 2 \times 10^6\delta t$ (c), and $t = 4 \times 10^6\delta t$ (d). Flow from left to right and periodic flow boundaries in all directions. Nonwetting phase blobs are shown in yellow (brighter color in gray scale), wetting phase in gray, and solid sites in black. $S_{nw} = 0.2$, $\mathrm{Bo} = 6.33 \times 10^{-2}$, $\lambda_s = \lambda_{nw} = 15\delta x$ [33].

as shown in Fig. 5(a) for $\mathrm{Bo} = 6.33 \times 10^{-2}$. During this period, both superficial velocities remain practically constant with time, although fluctuations around the average values may be significant. As expected, blob populations converge more slowly to their steady-state values than superficial velocities. Figure 5(b) shows the normalized fluctuations s of the blob phase velocity q_{nw} around the mean steady-state velocity, $s = q_{nw}/q_{nw}^{st}$. As described in more detail below, we attribute these velocity fluctuations to the blocking and unblocking events of the nonwetting phase blobs, which appear to be more pronounced at lower capillary numbers (resulting from lower applied Bond numbers), namely, stronger capillary over viscous forces across fluid-fluid interfaces.

It is worth noting here that, depending on the applied Bo value and the initial blob size distributions, the system required several million time steps δt to reach this "steady state". Typical simulations required approximately $3.5M\delta t$ and $20h$ on a massively parallel computer utilizing 64 physical processing cores (corresponding to $\sim$1300 cpu hours per simulation).

A. Dynamic blob breakup and coalescence

As discussed above, a key aspect of this type of flows lies in the coalescing and breaking-up events associated with blob trapping and deformation inside the media. In this section, we focus on the dynamics of those events. The evolution of the phase distribution patterns in Fig. 4 reveals that the NAPL phase flows primarily in the form of disconnected blobs that

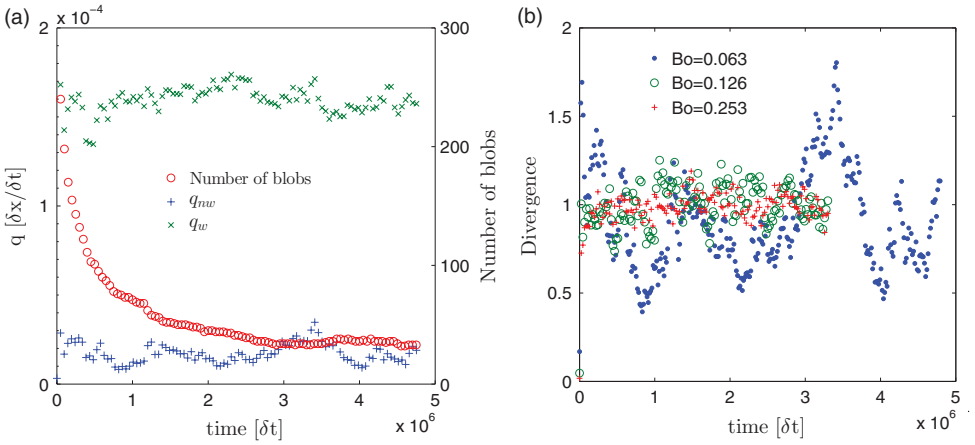

FIG. 5. (Color online) (a) Darcy phase velocities q for both phases and total blob population vs time t for Bo $= 6.33 \times 10^{-2}$, $S_{nw} = 0.2$, and $\lambda_s = \lambda_{nw} = 15\delta x$. (b) Normalized divergence $s = \frac{q_{nw}}{q_{nw}^{st}}$ of the superficial blob velocity q_{nw} with the respect to average steady-state value q_{nw}^{st} for different values of Bo.

occupy the central part of the pores. At the same time the wetting phase covers the pore walls forming a continuous liquid film that spans across the entire domain. The shape and population of the blobs are a function of the applied Bo number and S_{nw}.

At low Bo numbers, the blobs flow as long as their size is smaller than the average pore size. Starting from a large population of small blobs, as is the typical scenario in our simulations, the blobs flow at early times, and they continuously coalesce forming larger ones. For simplicity, we denote blob coalescence events as N−, as they result in a decrease of the overall population. These blobs progressively become immobile in smaller pore bodies, as viscous and gravity forces across fluid-fluid interfaces are not sufficiently strong to overcome capillarity and produce the required blob shape deformation to penetrate the pores. Eventually, at low Bo numbers the entire blob population becomes completely stranded (immobile), and only the flow of the wetting phase occurs in the pore space (see also Fig. 9(a) below). The dynamics of the process depend very strongly on the initial blob size distributions at low Bo values.

For intermediate Bo numbers, the blobs may be either mobile, as they enter higher permeability regions (larger pores), or immobile due to strong capillary forces in smaller pores. A careful inspection of the temporal evolution of the phase distribution patterns reveals that stronger Bo numbers lead to significant blob deformation and breaking up into smaller blobs. We denote breaking-up events as N+ , since they result in a increase of the population, and by $S_{nw,m}$ and $S_{nw,i}$, the saturations of the mobile and immobile blobs, respectively. These two populations exchange continuously mass between them through a series of N− and N+ events. As expected, larger blobs resulting from N− events have a higher probability of being mobile as they as subjected to stronger body and surface forces. Smaller blobs on the other hand, which are produced by N+ events, have a higher probability of being stranded.

Figure 6 presents the dynamics of these mechanisms for different Bo numbers. The plot shows the measured pairs of blobs coalescing (corresponding to N− events) and single blobs breaking up (corresponding to N+ events) in a fixed time interval $[t,t + \Delta t]$, where $\Delta t = 5 \times 10^4 \delta t$. The event numbers are normalized by the total blob population at time t, in order to express the event probabilities vs time. Alternatively, these could also be expressed as event rates by dividing event numbers by Δt. It is apparent here that during early times, when a very large population of smaller blobs exists, the process is mostly governed by blob collisions and N− events, while blob breaking up is negligible. As the overall population reduces and larger blobs are formed, a significant increase of the breaking up probability is observed. After sufficient time, the system reaches a dynamic equilibrium where the two probabilities become practically equal, but nonzero, revealing that the blobs undergo a continuous life cycle of N+ and N− events as they flow in this periodic boundary domain. The nonlinear nature of the blob flow process in porous media is also evident in Fig. 6 with respect to the applied Bo number. The steady-state rate of structural events decreases by more than one order of magnitude, as the applied Bond number is decreased only by a factor of 4.

To conclude this section, it is worth discussing briefly the physics behind the structural events that occur during the flow of NAPL blobs. Blob breaking up into smaller ones in porous media occurs when blobs reach smaller pores, and a significant

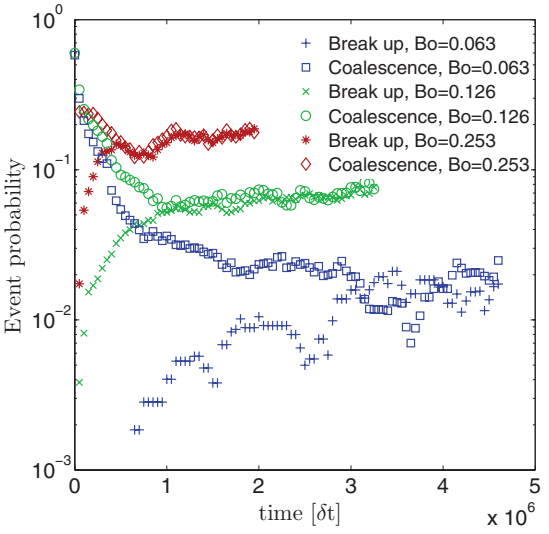

FIG. 6. (Color online) Probability of N+ and N− events for different values of the Bo number. $S_{nw} = 0.2$, $\lambda_s = \lambda_{nw} = 15\delta x$.

FIG. 7. (Color online) A sequence of snapshots focusing on a subdomain where N+ events commonly occur during the numerical simulation. A significant structural deformation of the original blob as it goes through a narrower pore leads to a N+ event. $S_{nw} = 0.2$, Bo $= 0.127$, $\lambda_s = 15\delta x$. Nonwetting phase blobs are shown in yellow (brighter color in gray scale), wetting phase in gray, and solid sites in black.

shape deformation is required in order to overcome capillary pressure entry values across pore throats. In order to invade these throats, the blobs respond to the normal and shear stresses acting on their interfaces by readjusting their shape, which can be characterized by the interfacial curvature. As a result, the curvature at the upstream side of the blobs decreases, and thus the capillary pressure across the leading part of their interface decreases, while curvatures at the downstream side increase, as the blobs elongate to go through the narrower throats [10,11]. After the leading part of the blob passes through the restriction, its radius of curvature begins to increase again. At this point the blob interface becomes unstable under the effect of capillarity-induced pressure gradients in the wetting fluid side of the interface. Eventually the leading part of the blob snaps off from the remaining part, possibly leading also to the trapping of the smaller upstream part [34]. The dynamics of blob breaking up is a function of several parameters, including the wetting phase capillary number, but also the viscosity ratio of the fluids $M = \mu_{nw}/\mu_w$ [35].

Figure 7 shows the temporal evolution of such an event for a solitary blob that reaches a narrower pore in a magnified region of the computational domain. Figure 8 shows a sequence of two N− events involving three neighboring blobs at a very low Bond number, where capillary forces at pores are expected to be dominant over gravity and viscosity. The average position of the center of mass of the three blobs in the direction of the applied body force is also indicated above each snapshot with an arrow. Initially, the larger blob fits perfectly in the containing pore. However, after two N− events, the resulting blob is too large, and it moves slowly upstream towards an adjacent larger pore in order to minimize the interfacial curvatures. This movement is accompanied by the spontaneous imbibition of the wetting phase into the smaller pore spaces that contained initially the blobs. Thus part of the interfacial energy released during these N− events is used to move the resulting blob upstream, in the direction opposite to the flow direction.

B. Steady-state blob populations

In this section we focus on the effects of the Bond number, the NAPL phase saturation, the initial blob size distribution, and the correlation length of the medium to steady-state blob populations. We focus particularly on the ratio of mobile to stranded or total blob populations which is of significant importance to NAPL recovery technologies.

Figure 9 shows characteristic snapshots of the phase distribution patterns at steady state for different Bo values. These snapshots reveal a series of qualitative differences in the population, the shape, and the mobility of the blobs. At low Bo values [Fig. 9(a)], and after an initial period of intense blob coalescence (see Fig. 6 above), all blobs become practically immobile and rounded, stranded by capillary forces that develop at the pores throats. The average size of the blobs at steady state then depends strongly on the initial blob size distribution and S_{nw}. This is also demonstrated in Fig. 10, which shows the blob size distributions at steady state for both the mobile and immobile blobs for different values of Bo. The results are averaged over several time steps (typically 10) from snapshots taken at 50k δt intervals.

As Bo increases, blobs become gradually mobile as they are subjected to an overall body force proportional to their

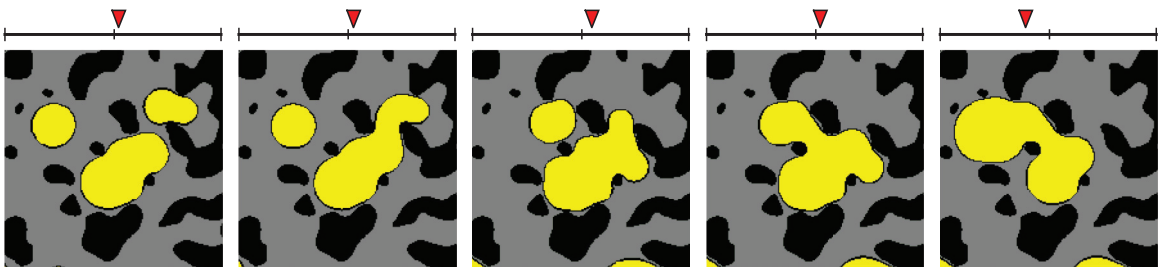

FIG. 8. (Color online) A sequence of snapshots focusing on a subdomain where a series of N− take place in the limit of capillarity-controlled process. The arrow above each snapshot shows the center of mass of the blobs in the flow direction. After each N− event, the produced larger blob cannot fit the initial pores and rearranges its shape by moving towards larger pores in order to reduce interfacial curvatures. In this case capillarity forces the larger blob upstream opposite to the direction of the applied body force. $S_{nw} = 0.2$, Bo $= 0.025$, $\lambda_s = 15\delta x$. Nonwetting phase blobs are shown in yellow (brighter color in gray scale), wetting phase in gray, and solid sites in black.

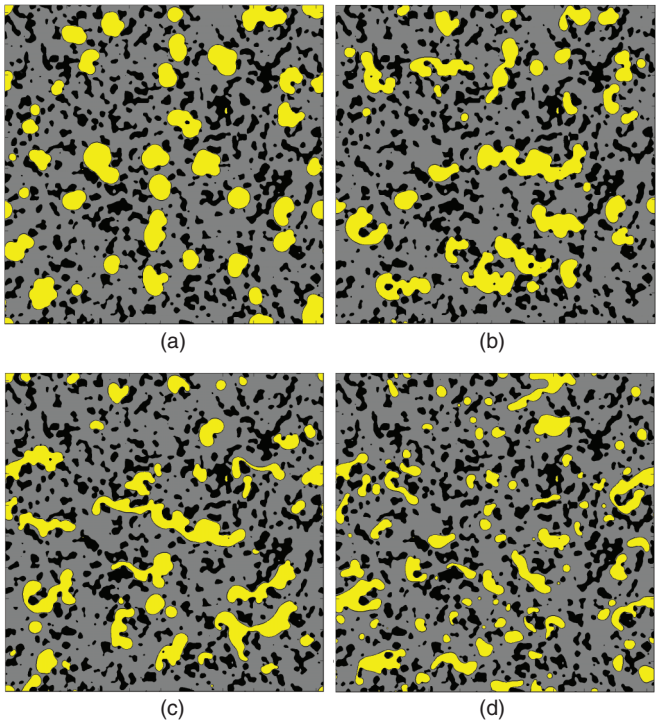

FIG. 9. (Color online) Phase distribution patterns at "steady-state" flow conditions for various values of the applied body force $\mathrm{Bo} = 2.53 \times 10^{-2}$ (a), $\mathrm{Bo} = 6.33 \times 10^{-2}$ (b), $\mathrm{Bo} = 1.27 \times 10^{-1}$ (c), and $\mathrm{Bo} = 2.53 \times 10^{-1}$ (d). A transition from immobile, practically circular blobs to elongated in the flow direction is clearly observed as the body force is increased. For low Bo values, the average blob size is limited by initial blob number density and saturation of the phase. For larger values, the average blob size is limited by the increased N+ probability. Nonwetting phase blobs are shown in yellow (brighter color in gray scale), wetting phase in gray, and solid sites in black.

size, but also stronger viscous forces at their interface by the flowing wetting phase. Under the effect of these forces blobs deform significantly, and they overcome capillary forces in pore throats [Figs. 9(b) and 9(c)]. In this intermediate Bo region, blobs coalesce at higher rates (see Fig. 6), and they elongate in the direction of the flow forming blobs that span several pore volumes.

In the higher Bo number region [Fig. 9(d)], viscous forces dominate over capillarity and dynamic breakup intensifies, producing larger populations of smaller blobs with size practically equal to average pore size.

The "steady-state" blob number density, namely, the number of produced blobs per unit volume of the porous medium (the averaging volume should be significantly larger than the average blob size to obtain statistically meaningful results), is of significant importance to physical processes occurring at interfaces, such as dissolution, evaporation, and reaction. In these processes, both the blob density and the specific interface, namely, the interface area per unit volume of the porous medium, are important. Figure 11(a) shows the average blob size $\bar{s}_b$ at "steady state" normalized by λ_s^2 vs the applied Bo number for various values of the NAPL-phase saturation and an initial blob size distribution with a correlation length $\lambda_{nw} = 15\delta x$. In the lower Bo region, most of the blobs are immobile, and the average size is determined by the initial distribution, or, equivalently, the flow history. The blob size increases with Bo as more blobs become mobile and the probability for N− events increases due to blob collisions. For even larger values of Bo, viscous forces take control over capillarity and the dynamic breakup of blobs intensifies, producing larger populations of smaller blobs. A clear maximum value for the blob size is found in the region $0.06 \leqslant \mathrm{Bo} \leqslant 0.07$. As expected larger nonwetting saturations produce larger blobs over the entire range of Bo values considered here.

Figure 11(b) shows the specific blob surface L_b, defined as the total interfacial area over the volume of the NAPL phase in the system, here in δx^2 units. A clear increase of L_b is evident with Bo resulting from the transition from practically rounded blobs at lower Bo values to elongated ones at intermediate values, and finally at increased blob populations in the upper Bo region. The effects of the initial blob size distribution are also demonstrated at low Bo and S_{nw} values.

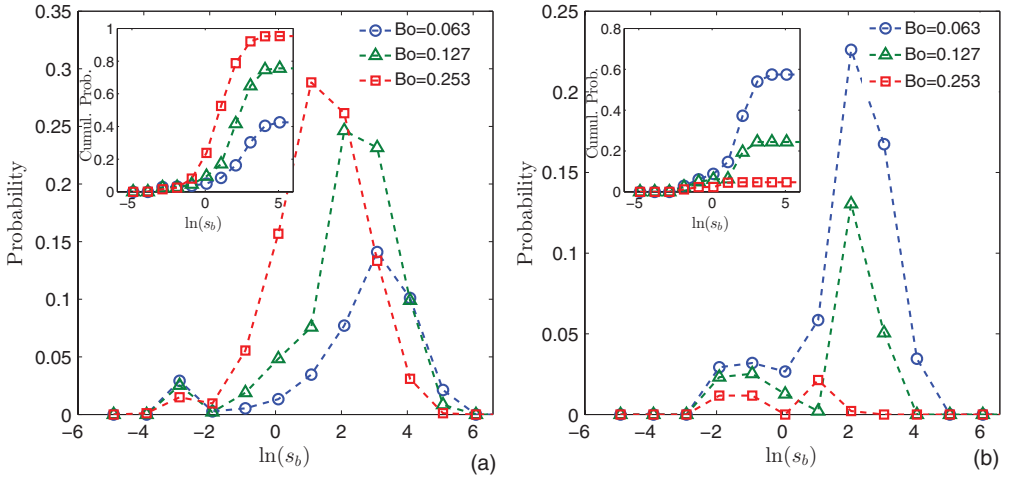

FIG. 10. (Color online) Steady-state blob size distributions for both mobile (a) and immobile populations (b) for different Bond numbers. The horizontal axis shows the natural logarithm of the blob size normalized by λ_s^2. Inlets show the corresponding cumulative distributions. $S_{nw} = 0.2$, $\lambda_{nw} = \lambda_s = 15\delta x$, $\phi = 0.8$.

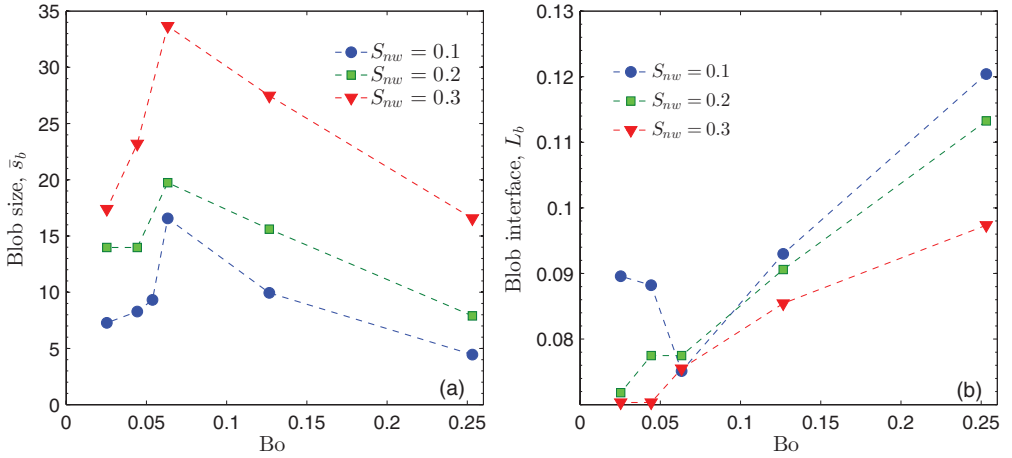

FIG. 11. (Color online) (a) Average blob size $\bar{s}_b$ in λ_{nw}^2 units vs the Bo number for different values of the nonwetting phase saturation S_{nw}. (b) Specific NAPL interface L_b, namely, total NAPL interface over the total NAPL phase volume, vs the Bo number. $\lambda_{nw} = \lambda_s = 15\delta x$, $\phi = 0.8$.

Figure 12 shows the ratio of mobile to the overall blob saturation $p_m = S_{nw,m}/S_{nw}$ with respect to the applied Bond number Bo for different values of S_{nw} and λ_{nw}. A sharp transition from a completely immobile blob population at lower Bo values is observed when a critical value $\mathrm{Bo_c}$ is exceeded. This indeed corresponds to a transition from single phase flow of the wetting phase in a medium of significantly decreased permeability (due to the pores blocked by the immobile blobs), to a two-phase flow regime where at least some of the blobs are mobile. Figure 12(b) supports the argument that larger correlation lengths λ_{nw}, thus larger blobs at $t = 0$, lead to progressively smaller values of $\mathrm{Bo_c}$. This is largely an anticipated result as larger blobs are subjected to stronger overall forces (in the form of both body forces and viscous stresses) and are thus mobilized at lower Bo values. This effect, however, was not studied thoroughly in our simulations, due to the relatively small size of the computational domain that did not allow for larger values of λ_{nw}, while pertaining a sufficiently large number of blobs for statistical purposes.

C. Flow regimes

It is expected that the mobility of NAPL blobs affects significantly the total flow of both phases in the porous domain by changing the "effective" permeability of the medium over a wide range of the applied Bo numbers. The presence of immobile blobs results in the blocking of some pores, excluding them from the flow paths available for the wetting phase. Therefore, the permeability of the medium, as "experienced" by the wetting phase, may be significantly decreased due to immobile blobs.

Recalling that the "effective" permeability of medium is the constant coefficient which relates flow rate to the applied pressure gradient, we plot in Fig. 13 the capillary number Ca, based on the total Darcy velocity $q = q_w + q_{nw}$ vs the Bond number Bo. At low Bo numbers, as discussed above, the ratio of mobile to total blob volume becomes $p_m \to 0$, and thus only the continuous wetting phase flows in the medium ($q \simeq q_w$). For these values of $\mathrm{Bo} < \mathrm{Bo_c}$ we find that the "effective" permeability of the medium is fixed, and there is linear Darcy-type dependence between Ca and Bo. This regime

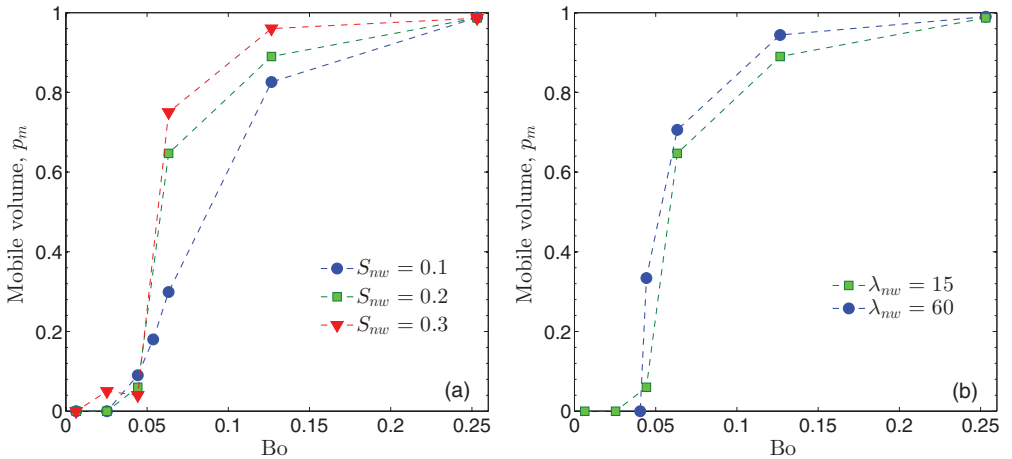

FIG. 12. (Color online) (a) Ratio $p_m = S_{nw,m}/S_{nw}$ of the mobile blob volume to the total nw-phase volume at steady state versus the applied Bo number for various values of S_{nw} and $\lambda_{nw} = 15\delta x$. (b) p_m vs the applied Bo number for different values of λ_{nw} and $S_{nw} = 0.2$.

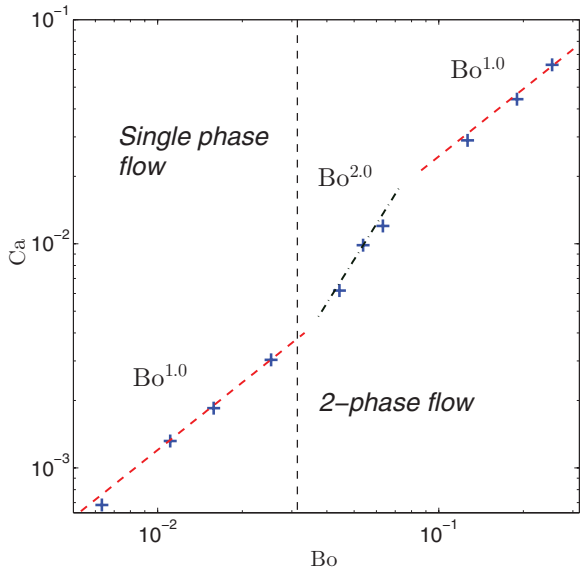

FIG. 13. (Color online) Flow regimes observed in this study expressed as $\mathrm{Ca} = q\mu_e/\gamma$ vs the Bond number $\mathrm{Bo} = g(\rho_w - \rho_{nw})\lambda_s^2/\gamma$. Symbols (+) show numerical simulation data. Red dashed lines represent a Darcy-type scaling where $\mathrm{Ca} \propto \mathrm{Bo}$, and the black dot-dashed line shows non-Darcy scaling where $\mathrm{Ca} \propto \mathrm{Bo}^2$. A transition from single phase flow (when all blobs are stranded) to two-phase flow occurs at a critical $\mathrm{Bo_c}$ value that is a function of the blob size.

effectively corresponds to single phase flow of the wetting phase in a medium of reduced, but constant, permeability due to pore blocking by the blobs.

This Darcy regime lasts until the threshold $\mathrm{Bo_c}$ (dashed-vertical line in Fig. 13) is exceeded, and the nonwetting blobs start to become mobilized. Above this threshold, more and more blobs are mobilized, and the flow of both phases is strongly influenced by capillarity. Therefore, a deviation from Darcy's law is expected [36–38]. Within this Bo range, a small increase in the applied body force, results in significant increase in the capillary number, as larger blobs are mobilized first, unblocking larger pore volumes that become part of the wetting phase flow paths (see also Fig. 12). We find that a scaling $\mathrm{Ca} \propto \mathrm{Bo}^2$ (dot-dashed line in Fig. 13) describes quite accurately the available numerical data in that region.

Increasing further the the applied Bo, when $p_m \to 1$, leads again to an almost linear relationship Darcy-type dependence between Ca and Bo, but with a larger (more than a factor of 2) prefactor compared to the regime below $\mathrm{Bo_c}$. Note that the prefactor is proportional to the effective permeability of the medium. In this last regime the average blob size becomes smaller than the average pore size and almost all blobs are mobile leading again to a Darcy's law for the mixture of wetting fluid and blobs with simultaneous occurrence of breaking up and coalescence (see Fig. 6).

Such behaviors are reminiscent of recent experimental and theoretical studies in immiscible pressure-driven flows [36–39]. Sinha *et al.* [39] proposed a robust theoretical explanation for the transition between these flow regimes based on a pore network representation of the medium. Using a pore network model, the flow in each pore throat is controlled by a capillary pressure threshold which depends on pore size and saturation. At the network scale this results in a pressure threshold for the total flow rate. As the pressure gradient increases, more pore throats become mobile (active) and thus contribute to the flow. Since each active throat contributes linearly with the applied pressure, while at the same time the number of active throats increases with the pressure drop, one should expect an exponent larger than one at lower Ca values. Based on a mean field approach, Tallakstad *et al.* [36] first showed that the flow rate scales as $q \propto (\Delta P)^2$ in this flow regime. This relationship was further generalized by Sinha *et al.* [39], who showed that the flow rate scales as $q \propto (\Delta P - \Delta P_c)^2$ close to ΔP_c, and as $q \propto \Delta P$ when $\Delta P \gg \Delta P_c$, where ΔP_c is the total capillary pressure threshold for the entire network. The non-Darcy regime is a consequence of the spatial distribution of the local pressure thresholds, when capillarity controls the process. It is also interesting to note that the transition from the capillarity-dominated to the viscosity-dominated regime at higher Bo values is found in our simulations to occur at $\mathrm{Ca} \simeq 0.03$, in good agreement with the theoretical predictions by Sihna *et al.* [39].

We should note, however, that the above model differs significantly from the one presented here. In our simulations, we solve explicitly for the interfacial dynamics within pore volumes, without assigning capillary pressure thresholds in the medium. Effectively, we solve the flow problem using a modified Navier-Stokes equation in the reconstructed medium. More importantly, our model accounts explicitly for snap-off and coalescence events, which are, as we have shown, a key issue in immiscible two-phase flows in porous media. This comparison, however, with previous studies reveals that the model presented here captures quite accurately the scaling between Ca and Bo that emanates from capillarity and the spatially random pore size distribution in porous media.

IV. CONCLUSIONS

In this paper we studied pore scale phenomena occurring during the immiscible flow of Non-Aqueous Phase Liquids (NAPLs) in 2D stochastically reconstructed porous domains. We employ a lattice Boltzmann model to simulate the dynamics of NAPL blobs as they flow through the porous medium, coupled with a Hoshen-Koppelman algorithm to determine the structural characteristics and mobility of the blob population. The process is characterized by two dimensionless numbers: the Bo and capillary Ca numbers, which express the interplay between capillary, viscous, and gravity forces. We find that the process is governed by the dynamical coalescence and breaking up of blobs, which result in two interacting populations of mobile and stranded blobs, which continuously exchange mass between them. At steady state, when the rates of blob breaking up and coalescing become equal, both populations follow a log-normal size distribution with an average size and cumulative volume that depends strongly on the applied Bo number. At higher Bo values, the ratio of mobile to stranded blob saturation increases significantly, as gravity forces overcome capillarity as fluid-fluid interfaces move through pore bodies, and the breaking rate increases, leading to smaller blob sizes. Our simulations show that the transition between single and two-phase flow occurs when a critical value of Bo is applied, and then the mobile blob volume

increases nonlinearly with Bo until viscous forces become dominant in the system. Three flow regimes are identified: a single-phase Darcy-type regime at low Bo numbers, a non-Darcy two-phase flow regime at intermediate values of Bo where the capillary number scales as $\mathrm{Ca} \propto \mathrm{Bo}^2$, and a Darcy-type two-phase regime at higher values of Bo. These results are in good agreement with recent experimental and theoretical works.

ACKNOWLEDGMENTS

The work of A.G.Y. is supported by the EU funded Grant "Real Pore Flows" Contract No. 254804 under call FP7-PEOPLE-IEF2009. Funding was also provided by the Initial Training Network "Multiflow" Contract No. GA-2008-214919. This work was performed using HPC resources from GENCI-IDRIS (Grant No. 2011-26668). We acknowledge useful discussions with Alex Hansen.

[1] F. Orr and J. Taber, Science **224**, 563 (1984).
[2] K. Lackner, Science **300**, 1677 (2003).
[3] J. McGray, G. Tick, J. Jawitz, J. Gierke, M. Brusseau, R. Falta, R. Knox, D. Sabatini, M. Annable, J. Harwell *et al.*, Ground Water **49**, 727 (2011).
[4] M. Dias and A. Payatakes, J. Fluid Mech. **164**, 305 (1986).
[5] M. Dias and A. Payatakes, J. Fluid Mech. **164**, 337 (1986).
[6] G. Constantinides and A. Payatakes, AIChE J. **42**, 369 (1996).
[7] G. Wagner, A. Birovljev, P. Meakin, J. Feder, and T. Jøssang, Phys. Rev. E **55**, 7015 (1997).
[8] J. Schmittbuhl, A. Hansen, H. Auradou, and K. J. Måløy, Phys. Rev. E **61**, 3985 (2000).
[9] H. Auradou, K. J. Måløy, J. Schmittbuhl, and A. Hansen, Transp. Porous Media **50**, 267 (2003).
[10] K. M. Ng and A. C. Payatakes, AIChE J. **26**, 419 (1980).
[11] A. C. Payatakes, K. M. Ng, and R. W. Flumerfelt, AIChE J. **26**, 430 (1980).
[12] M. Valavanides, G. Constantinides, and A. Payatakes, Trans. Porous Media **30**, 267 (1998).
[13] P. Amili and Y. Yortsos, Trans. Porous Media **64**, 25 (2006).
[14] C. Pan, M. Hilpert, and C. T. Miller, Phys. Rev. E **64**, 066702 (2001).
[15] C. Pan, M. Hilpert, and C. Miller, Water Resour. Res. **40**, W01501 (2004).
[16] T. Ramstad, N. Idowu, C. Nardi, and P.-E. Oren, Trans. Porous Media **94**, 487 (2012).
[17] X. He, X. Shan, and G. D. Doolen, Phys. Rev. E **57**, R13 (1998).
[18] T. Lee and C. Lin, J. Comput. Phys. **206**, 16 (2005).
[19] E. S. Kikkinides, A. G. Yiotis, M. E. Kainourgiakis, and A. K. Stubos, Phys. Rev. E **78**, 036702 (2008).
[20] J. Rowlinson and B. Widom, *Molecular Theory of Capillarity*, 2nd ed. (Dover Publications, Mineola, NY, 2003).
[21] X. He, S. Chen, and R. Zhang, J. Comput. Phys. **152**, 642 (1999).
[22] A. J. Wagner, Phys. Rev. E **74**, 056703 (2006).
[23] V. Bongiorno and H. Davis, Phys. Rev. A **12**, 2213 (1975).
[24] T. Lee and P. F. Fischer, Phys. Rev. E **74**, 046709 (2006).
[25] S. Succi, *The Lattice Boltzmann Equation for Fluid Dynamics and Beyond* (Oxford University Press, Oxford, 2001).
[26] I. Ginzburg and D. d'Humières, Phys. Rev. E **68**, 066614 (2003).
[27] C. Pan, L.-S. Luo, and C. T. Miller, Computers Fluids **35**, 898 (2006) [in Proceedings of the First International Conference for Mesoscopic Methods in Engineering and Science].
[28] L. Talon, D. Bauer, N. Gland, S. Youssef, H. Auradou, and I. Ginzburg, Water Resour. Res. **48**, W04526 (2012).
[29] A. G. Yiotis, J. Psihogios, M. E. Kainourgiakis, A. Papaioannou, and A. K. Stubos, Colloids Surf. A **300**, 35 (2007) [4th International TRI/Princeton Workshop, Princeton, NJ, 21–23 June 2006].
[30] P. Adler, C. Jacquin, and J. Quiblier, Int. J. Multiphase Flow **16**, 691 (1990).
[31] M. E. Kainourgiakis, T. A. Steriotis, E. S. Kikkinides, G. C. Charalambopoulou, J. D. F. Ramsay, and A. K. Stubos, Chem. Phys. **317**, 298 (2005).
[32] J. Hoshen and R. Kopelman, Phys. Rev. B **1**, 3438 (1976).
[33] See Supplemental Material at http://link.aps.org/supplemental/10.1103/PhysRevE.87.033001 for the full movie of the numerical simulation for 6.6Mδt with phase distribution snapshots taken at 50kδt intervals.
[34] P. Gauglitz and C. Radke, J. Colloid Interface Sci. **134**, 14 (1990).
[35] D. Avraam and A. Payatakes, J. Fluid Mech. **293**, 207 (1995).
[36] K. T. Tallakstad, H. A. Knudsen, T. Ramstad, G. Løvoll, K. J. Måløy, R. Toussaint, and E. G. Flekkøy, Phys. Rev. Lett. **102**, 074502 (2009).
[37] K. T. Tallakstad, G. Løvoll, H. A. Knudsen, T. Ramstad, E. G. Flekkøy, and K. J. Måløy, Phys. Rev. E **80**, 036308 (2009).
[38] P. Sharma, P. Aswathi, A. Sane, S. Ghosh, and S. Bhattacharya, Soft Matter **8**, 5791 (2012).
[39] S. Sinha and A. Hansen, Europhys. Lett. **99**, 44004 (2012).